

CineMA: A Foundation Model for Cine Cardiac MRI

Yunguan Fu^{a,b}, Weixi Yi^a, Charlotte Manisty^c, Anish N Bhuvan^{c,d},
Thomas A Treibel^{c,d}, James C Moon^c, Matthew J Clarkson^a,
Rhodri Huw Davies^c, Yipeng Hu^a

^a*UCL Hawkes Institute, University College London, UK*

^b*InstaDeep, UK*

^c*Institute of Cardiovascular Sciences, University College London, UK*

^d*Barts Heart Centre, Barts Health NHS Trust, UK*

Abstract

Background Cardiac magnetic resonance (CMR) is a key investigation in clinical cardiovascular medicine and has been used extensively in population research. However, extracting clinically important measurements such as ejection fraction (EF) for diagnosing cardiovascular diseases remains time-consuming and subjective. We developed CineMA, a foundation AI model automating these tasks with limited labels.

Methods CineMA is a self-supervised autoencoder model trained on 74,916 cine CMR studies to reconstruct images from masked inputs. After fine-tuning, it was evaluated across eight datasets on 23 tasks from four categories: ventricle and myocardium segmentation, left and right ventricle ejection fraction (LVEF, RVEF) calculation, disease detection and classification, and landmark localisation. Models and code for pre-training and fine-tuning are available at <https://github.com/mathpluscode/CineMA>.

Findings CineMA is the first foundation model for cine CMR to match or outperform convolutional neural networks (CNNs). CineMA predicted more accurate EF from segmentation (LVEF mean absolute error [MAE] 3.33%, 2.88%–3.82%); RVEF MAE 5.49%, 4.74%–6.55%), outperforming CNN (3.63 [2.99–4.24]% and 6.28 [5.33–7.48]%, respectively). On datasets not used during training, CineMA obtained reduced error (MAE 4.83%, 4.58%–5.21%) and coefficient of variation (8.45%, 7.43%–9.30%) compared to CNN (5.59 [5.23–6.01]% and 12.02 [10.73–13.19], respectively). With 50% labels, CineMA retained comparable performance. For detecting and diagnosing

diseases, CineMA achieved a substantially higher specificity (60.06%, 52.23%–68.73%) than CNN did (31.55%, 22.92%–39.98%), and improved sensitivity (90.20%, 85.77%–93.64% vs. 86.84%, 83.85%–89.44%).

Interpretation CineMA demonstrated greater label efficiency than CNNs, achieving comparable or better performance with fewer annotations. This reduces the burden of clinician labelling and supports replacing task-specific training with fine-tuning foundation models in future cardiac imaging applications. Code release democratises access to high-performance models that otherwise require substantial computational resources, promoting reproducibility and accelerating clinical translation.

Funding National Institute for Health and Care Research. University College London Hospitals Biomedical Research Centre.

Keywords: artificial intelligence, foundation model, cardiovascular disease, segmentation, ejection fraction, cardiac magnetic resonance imaging

1. Introduction

Despite major advances over the last few decades, cardiovascular diseases (CVDs) remain the leading cause of mortality worldwide, accounting for over 17.9 million deaths annually [1]. Many clinical decisions in disease diagnosis are driven by imaging assessment of cardiac size, structure, and function. Due to high accuracy, tissue contrast, non-invasiveness, and non-ionising nature, cardiovascular magnetic resonance (CMR) is now an integral part of many international guidelines [2, 3]. Cine imaging, the cornerstone of cardiac MRI, enables assessing cardiac size (e.g., cavity volume), mass (e.g., left ventricle [LV] mass), global systolic function (e.g., left ventricle ejection fraction [LVEF]), and long-axis function (e.g., mitral annular plane systolic excursion [MAPSE], and global longitudinal shortening [GLS]). CMR is established as the gold standard for estimating these measures and providing both diagnostic (e.g., heart failure with reduced ejection fraction) and prognostic information [4]. However, interpreting CMR images and deriving biomarkers for diagnosis, monitoring, and prognostication remain labour-intensive tasks that require experienced clinicians. In addition, the annotation process is inherently subjective, contributing to substantial intra- and inter-observer variability [5], which can affect clinical decision-making and compromise consistency in patient care.

With the advancement of deep learning in artificial intelligence, automated image interpretation has become feasible, helping to alleviate clinician workload and improve clinical workflow efficiency. However, these models typically require large expert-annotated datasets, representing similar challenges and pitfalls to the above-discussed manual interpretation. UK Biobank (UKB) [6] includes large CMR image and medical record collections, but it lacks task-specific labels for downstream applications. Other CMR datasets (see Appendix B) are also accessible, but their size and diversity remain limited.

Foundation models [7], models trained with self-supervision and adaptable to diverse downstream tasks, thus hold potential for advancing CMR imaging analyses. These models require no manual annotations and can be fine-tuned with limited labels. MedSAM [8] is one example of a successful 2D medical image segmentation model that was evaluated on CMR data. However, it requires bounding box inputs for all training data, which remain labour-intensive to produce. Several preprints have recently proposed foundation models tailored specifically to CMR [9, 10, 11]. Shad et al. [9] developed a video foundation model for predicting LVEF and detecting and diagnosing diseases, while Jacob et al. [10] introduced a 2D model evaluated on disease detection, ventricle segmentation, and landmark localisation. More recently, Zhang et al. [11] proposed a multi-modal foundation model by aligning image embeddings with tabular features and was evaluated on ejection fraction (EF) regression and disease classification tasks.

We present CineMA, a cine CMR foundation model using the self-supervised masked autoencoder framework [12], trained on 74,916 cine CMR studies from UKB. We hypothesised that pre-training on large-scale unlabeled cine CMR data would enable the model to learn transferable representations, providing a strong foundation for downstream tasks. Fine-tuned variants of CineMA could thus outperform models trained from random initialisation when provided with the same amount of labelled data, or achieve comparable performance using substantially fewer annotations.

To evaluate the utility of CineMA, we tested a range of clinically relevant tasks, including ventricle and myocardium segmentation, direct ejection fraction regression, disease detection and classification, and landmark localisation. These tasks represent different components of cardiac image interpretation in routine practice. Ventricular segmentation enables chamber volume quantification, which is essential for estimating ejection fraction—a key functional biomarker used to assess systolic function, inform prognosis and treatment de-

cisions. Cardiovascular disease detection and classification support automated diagnostic triage and disease stratification. Localisation of landmarks such as mitral annular and apical points allows the measurement of MAPSE and GLS, both of which reflect longitudinal function of the heart, which is an important contributor to overall systolic function [13]. Overall, CineMA was evaluated across 23 tasks using eight datasets comprising over 4,000 cine CMR images, including both SAX and LAX views (see Table B.2), to our best knowledge, representing the most comprehensive evaluation of machine learning models in CMR to date. CineMA is also the first foundation model to demonstrate superior or comparable performance across a broad spectrum of clinically relevant cine CMR tasks. All code for pre-training, fine-tuning, and evaluation, along with weights of pre-trained and fine-tuned models, are publicly available under an MIT license at <https://github.com/mathpluscode/CineMA>.

Research in context

Evidence before this study

We searched PubMed and arXiv up to April 18, 2025, using “cardiac” and “foundation model”, and identified 29 studies on cardiac vision models. Eight studies focused on cardiac magnetic resonance (CMR), and only three were cine CMR models trained on large-scale datasets (>20,000 studies) and evaluated on multiple downstream tasks, but none of these three studies had yet been peer-reviewed at the time of writing. Notably, no prior work has assessed model consistency across repeated acquisitions, generalisation to out-of-distribution datasets concerning both pre-training and fine-tuning, or the quantitative benefits of foundation models under limited training data—key aspects for clinical deployment.

Added value of this study

CineMA is the first cine CMR foundation model to consistently match or outperform convolutional neural networks trained from random initialisation, across multiple clinically relevant tasks—evaluated over 23 tasks across eight datasets. CineMA improved boundary delineation in segmentation and provided more reliable ejection fraction estimates. It also showed stronger generalisation to out-of-distribution data and maintained performance with only 50% of the annotations. For detecting and diagnosing diseases, CineMA demonstrated higher specificity and sensitivity. To support reproducibility and clinical adoption, all pre-training and fine-tuning code, model weights, and inference scripts are released at the time of submission.

Implications of all the available evidence

Together with prior studies, this work supports a paradigm shift from developing isolated, task-specific models to fine-tuning general-purpose backbones. By open-sourcing model weights and code, CineMA lowers barriers to high-performance model access, promoting reproducibility and broader adoption. This enables capabilities previously limited by data or resource constraints and lays the foundation for future work in expanding to other modalities, leveraging temporal and multi-modal data, and assessing clinical impact in prospective studies.

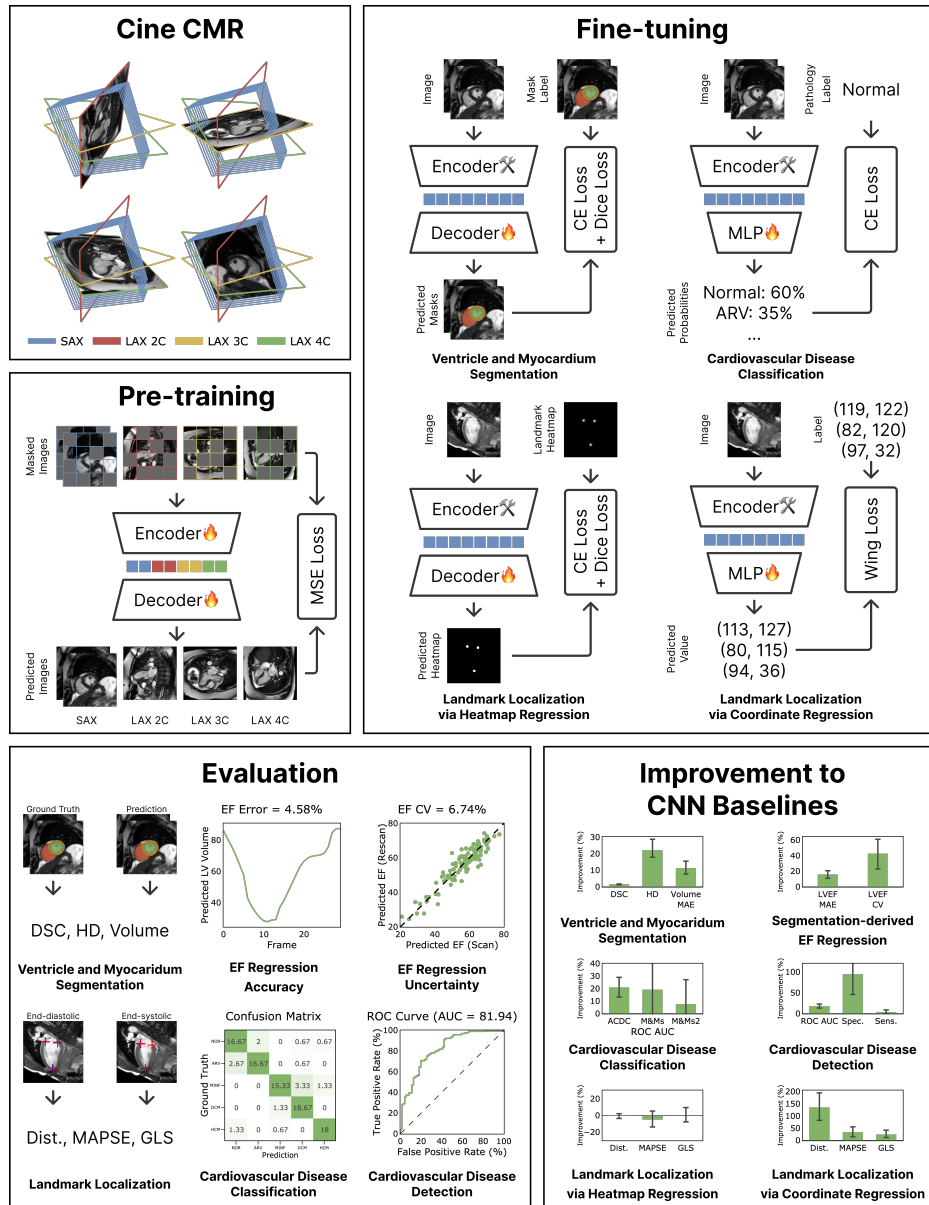


Figure 1: Summary of CineMA pre-training, fine-tuning, evaluation, and results. fire=trained from random initialisation. hammer-and-wrench=fine-tuned. SAX=short-axis. LAX=long-axis. 2C=two-chamber. 3C=three-chamber. 4C=four-chamber. CE=cross entropy. MLP=multilayer perceptron. CNN=convolutional neural network. DSC=Dice score. HD=95th percentile Hausdorff distance. Dist.=distance. EF=ejection fraction. CV=coefficient of variation. ROC=receiver operating characteristic. AUC=area under curve. Spec.=specificity. Sens.=sensitivity. MAPSE=mitral annular plane systolic excursion. GLS=global longitudinal shortening.

2. Methods

2.1. Study design and data

This study utilised nine datasets for model development and evaluation, summarised in Appendix B. CineMA was pre-trained using a masked image reconstruction task on cine CMR images from UKB, incorporating all four standard views—two-chamber (2C), three-chamber (3C), four-chamber (4C) LAX, and SAX. Ventricle and myocardium segmentation, and ejection fraction regression tasks, were evaluated on ACDC [14], M&Ms [15], and M&Ms2 [16] datasets. EF was both derived from ventricle volumes using segmentation models and directly estimated using image-based regression models. Segmentation models were further evaluated for LVEF regression on the Kaggle [17] and Rescan [5] datasets, which were not used during pre-training and fine-tuning. These analyses assess the model’s zero-shot (i.e., without any further training) generalisability on out-of-distribution data. Model consistency across repeated scans was also evaluated on Rescan dataset. For diagnosing disease subtypes, models were trained and evaluated independently on ACDC, M&Ms, and M&Ms2 datasets, followed by a pooled evaluation for binary classification of disease presence. Landmark localisation was assessed using paired LAX 2C and 4C images from the Landmark dataset [18]. Two strategies were compared: segmentation-like heatmap regression and direct coordinate regression. To evaluate the transferability of CineMA beyond cine CMR, we tested the model on EMIDEC [19] and MyoPS2020 [20], both tasked for scar segmentation based on late gadolinium enhancement (LGE) imaging.

2.2. CineMA model development

CineMA used the masked autoencoder framework [12] to reconstruct images from masked inputs. CineMA incorporated convolutional encoders inspired by ConvMAE [preprint] [21] to reduce memory consumption. To support multi-view cine CMR inputs, CineMA adopted MultiMAE [22], enabling independent encoding and decoding of each view. The architecture is detailed in Appendix C.1 and illustrated in Figure C.5. The model was pre-trained for 800 epochs using mean squared error for masked image reconstruction on 74,916 cine CMR images from the UK Biobank (up to November 6, 2023) [6]. The pre-training was completed in 18 days on 8 NVIDIA RTX A6000 GPUs on the University College London Computer Science HPC cluster. Training details are provided in Appendix C.3.

2.3. Downstream task evaluation

Three configurations were compared per task: (1) a convolutional neural network trained from random initialisation—ResNet-50 [23] (denoted ResNet) for tasks involving tabular labels (e.g., disease classes, EF, and landmark coordinates), or UNet for pixel- or voxel-wise tasks (e.g., segmentation or landmark heatmap prediction); (2) CineMA, the fine-tuned version of the pre-trained model (see Appendix C.1, fine-tuned models in different tasks are denoted CineMA for simplicity); and (3) a model with the same architecture as fine-tuned models but trained from random initialisation (denoted CineMA^{Rand}). All models were trained three times using different random seeds, on the full dataset or defined subsets. Model fine-tuning was performed on the University College London Computer Science HPC cluster and Isambard-AI cluster [24]. Full training configurations are described in Appendix C.4.

The UNet-based baseline models were used as they demonstrated competitive performance for segmentation [10] and landmark localisation [18]. The nnUNet [25] was not included in benchmarks due to its automated optimisation pipeline. Fair comparison with such an AutoML optimisation to foundation models remains an open research direction.

Segmentation performance was assessed using Dice score, 95th percentile Hausdorff distance, and mean absolute error (MAE) for volume estimation. When applicable, EF was derived from estimated ventricular volumes. To evaluate model consistency across repeated acquisitions, coefficient of variation was calculated on paired images from Rescan dataset. Regression tasks were evaluated using MAE. The classification was evaluated using the area under the receiver operating characteristic curve (ROC AUC), and for disease detection, sensitivity and specificity were reported. Landmark localisation accuracy was evaluated using Euclidean distance, MAPSE and GLS, metrics quantifying longitudinal cardiac function.

2.4. Statistical analysis

To estimate 95% confidence intervals (CI), we applied bootstrapping on each test set by sampling N examples with replacement ($N =$ test set size). Metrics were averaged across the three trained model checkpoints for each bootstrap sample, and this process was repeated 100 times to compute the mean and 95% CI (2.5th percentile–97.5th percentile). Statistical significance was evaluated using two-sided t-tests on the bootstrapped metric values, at

varying significance levels, denoted *** for $p < 0.001$, ** for $p < 0.01$, and * for $p < 0.05$; ns indicates non-significance.

3. Results

3.1. CineMA improved segmentation and EF estimation accuracy

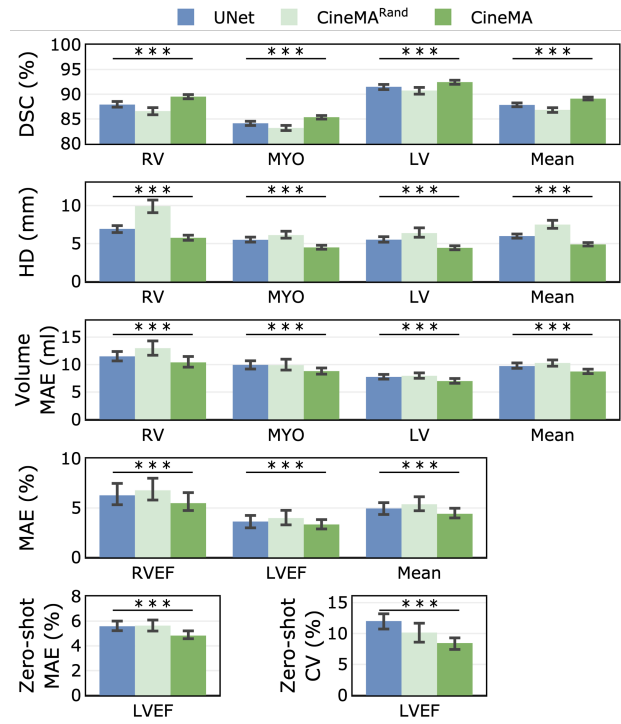
CineMA consistently improved ventricles and myocardium segmentation across ACDC, M&Ms, and M&Ms2 datasets. It achieved a mean Dice score of 89.11 (88.84–89.42)% on the combined hold-out test sets, outperforming both the UNet (87.84 [87.47–88.24])% and the CineMA^{Rand} (86.84 [86.32–87.27])% (see Figure 2a; detailed per-dataset results are summarised in Figure D.7a). CineMA also yielded the lowest 95th percentile Hausdorff distance of 4.89 (4.68–5.13) mm, compared to 5.98 (5.71–6.26) mm for UNet and 7.49 (7.00–8.06) mm for CineMA^{Rand}, indicating consistently superior boundary delineation. Example predictions are shown in Figure 3.

Improved segmentation accuracy yielded more precise ventricular volume estimates, with CineMA yielding MAEs of 7.00 (6.60–7.46) ml for LV and 10.40 (9.53–11.47) ml for RV, outperforming UNet (7.75 [7.35–8.21] ml and 11.50 [10.66–12.38] ml, respectively). Consequently, CineMA provided more accurate EF estimates from segmentation-derived volumes, achieving MAEs of 3.33 (2.88–3.82)% for LVEF and 5.49 (4.74–6.55)% for RVEF, compared to UNet (3.63 [2.99–4.24]% and 6.28 [5.33–7.48]%, respectively) and CineMA^{Rand} (3.98 [3.29–4.76]% and 6.78 [5.80–8.01]%, respectively). These results demonstrated CineMA’s ability to produce clinically reliable EF measurements through improved segmentation accuracy.

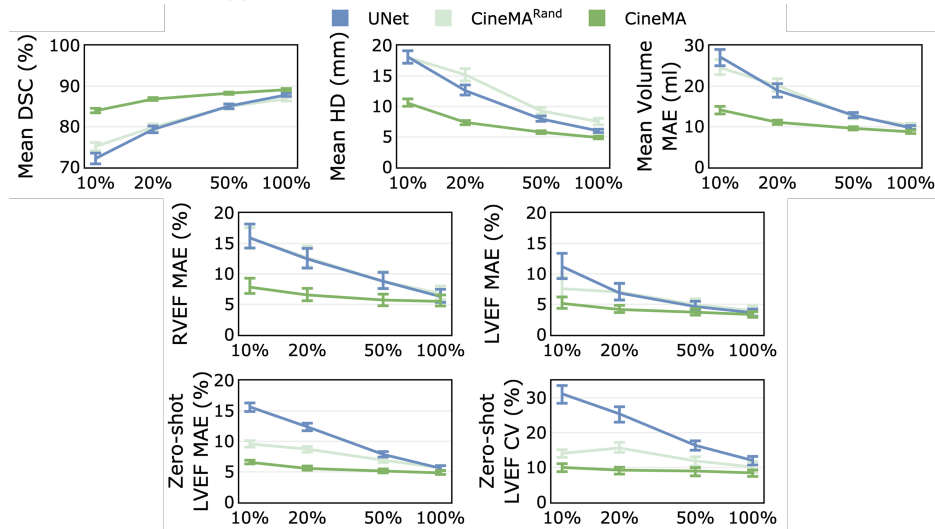
CineMA was also evaluated on direct LVEF regression without segmentation supervision. It achieved MAE of 5.21 (4.7–5.71)%, outperforming both CineMA^{Rand} and ResNet (see Figure D.13a and Table D.11). However, compared to segmentation models, these models exhibited higher errors and lacked visual interpretability, which may limit their clinical applicability.

3.2. CineMA increased accuracy and consistency in zero-shot LVEF estimation

To assess generalisability, CineMA was evaluated in a zero-shot setting—predicting LVEF on images from Kaggle and Rescan datasets without any additional training. These two datasets were not used in pre-training or fine-tuning. CineMA achieved the lowest LVEF MAE of 4.83 (4.58–5.21)%, outperforming both the UNet (5.59 [5.23–6.01]%) and CineMA^{Rand} (5.64% [5.20–6.09]%) (see



(a) Models trained with all available training data.



(b) Models trained with a subset of available training data.

Figure 2: Segmentation evaluation. UNet and CineMA^{Rand} were trained from random initialisation, while CineMA was fine-tuned. DSC=Dice score. HD=95th percentile Hausdorff distance. RV=right ventricle. MYO=myocardium. LV=left ventricle. EF=ejection fraction. CV=coefficient of variation. MAE=Mean absolute error.

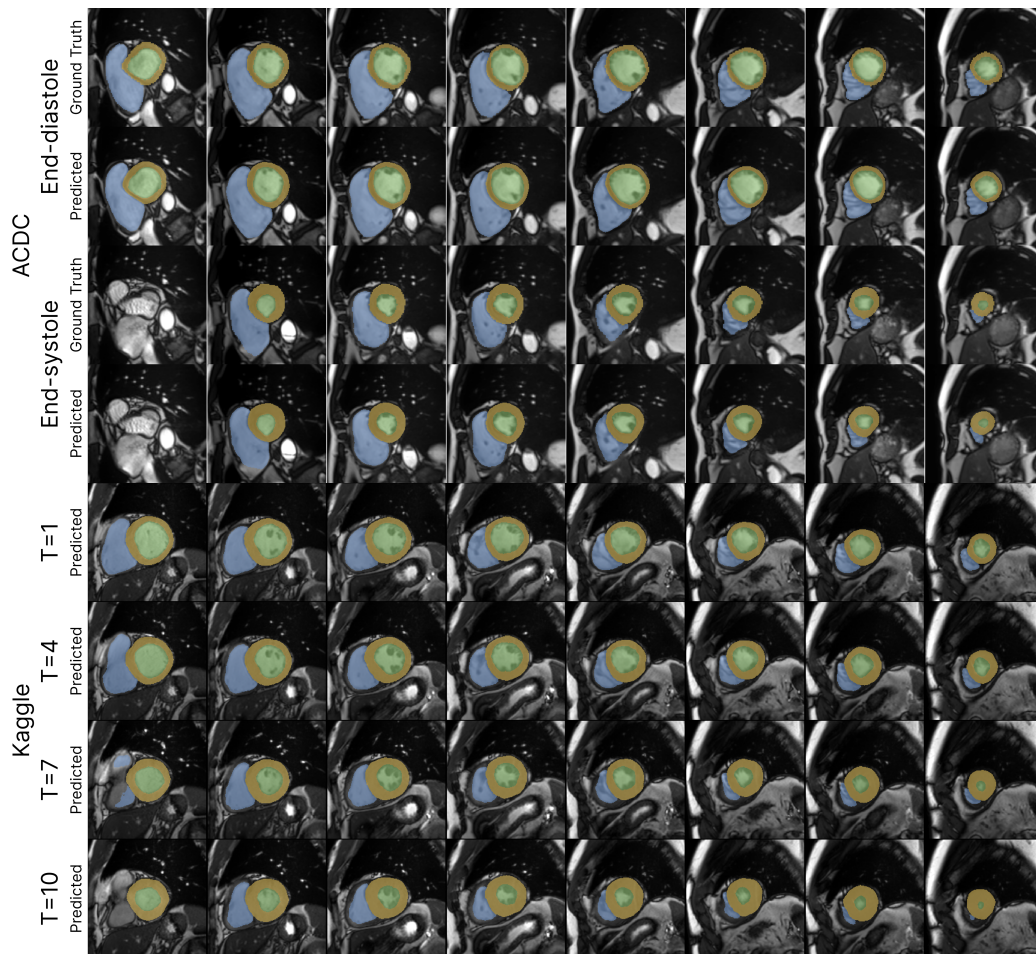


Figure 3: Example segmentations on ACDC and Kaggle dataset test splits. The segmentation model was a fine-tuned version of CineMA using ACDC dataset. The model was not trained on Kaggle dataset. Each column corresponds to a SAX slice.

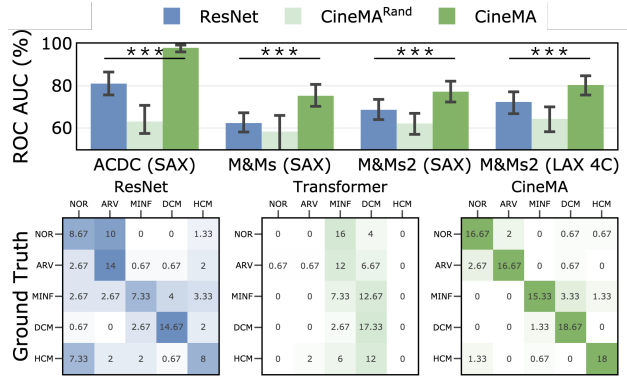
Figure 2a; detailed per-dataset results in Figure D.7). Example predictions are illustrated in Figure 3. The robustness of CineMA was further supported by its enhanced consistency on Rescan dataset. CineMA achieved a coefficient of variation of 8.45 (7.43–9.30)% across paired scans, lower than the UNet (12.02 [10.73–13.19]) and CineMA^{Rand} (10.16 [8.60–11.67]), highlighting its superior consistency. These reductions in both error and variability indicate that CineMA provides more accurate and consistent EF regression on data distributions that were unseen previously during pre-training and fine-tuning, suggesting its potential utility in real-world clinical workflows, particularly for longitudinal patient monitoring.

3.3. CineMA maintained segmentation accuracy with half the training data

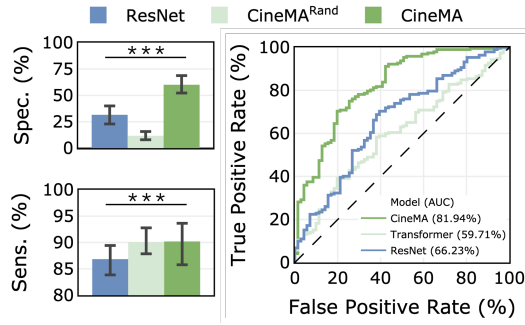
CineMA was evaluated under reduced annotation conditions to assess sample efficiency. As illustrated in Figure 2b, the advantage of CineMA became increasingly pronounced across all metrics as the quantity of training data decreased. Notably, with only 50% of the training data, CineMA achieved a mean Dice score of 88.26 (87.96–88.53)%, a mean 95th percentile Hausdorff distance of 5.78 (5.55–6.01) mm, and a mean volume MAE of 9.60 (9.2–10.0), outperforming UNet trained on the full dataset (see Figure 2b). For segmentation-derived EF regression, CineMA with 50% data achieved MAEs of 3.72 (3.24–4.27)% for LVEF and 5.72 (4.77–6.68)% for RVEF. Compared to the UNet model trained on the entire dataset, CineMA demonstrated essentially comparable performance for LVEF (difference = 0.09%) and lower error for RVEF (difference = 0.56%). Of note, CineMA’s zero-shot generalisation performance remained robust even when trained on reduced data. With 50% and 20% of training data, LVEF MAEs on Kaggle and Rescan datasets were 5.14 (4.83–5.48)% and 5.56 (5.27–5.95)%, respectively, both lower than UNet’s 5.59 (5.23–6.01)% trained on the full dataset. Similarly, the coefficient of variation for CineMA was 8.99 (7.59–9.97)% with 50% data and 9.24 (8.12–10.09)% with 20% data, lower than 12.02 (10.73–13.19)% for UNet trained with all labeled data. These findings highlight CineMA’s ability to retain strong segmentation and EF regression accuracy even in low-data settings, demonstrating its value in reducing manual annotation burdens while preserving clinical reliability.

3.4. CineMA enhanced disease detection and diagnosis

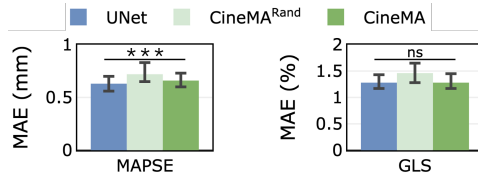
Cardiovascular disease diagnosis was evaluated through subtype classification on ACDC, M&Ms, and M&Ms2 datasets separately, each contain-



(a) Cardiovascular disease subtype classification. The confusion matrices were on ACDC.



(b) Disease detection



(c) Valve and apical landmarks localisation

Figure 4: Evaluation of cardiovascular diseases detection and diagnosis, and landmark localisation. ResNet, UNet and CineMA^{Rand} were trained from random initialisation, while CineMA was fine-tuned. NOR=normal. ARV=abnormal right ventricle. MINF=myocardial infarction. DCM=dilated cardiomyopathy. HCM=hypertrophic cardiomyopathy. Spec.=specificity. Sens.=sensitivity. AUC=Area under the receiver operating characteristic curve. MAPSE=mitral annular plane systolic excursion. GLS=global longitudinal shortening. MAE=mean absolute error.

ing different diagnostic labels. CineMA consistently outperformed both the CineMA^{Rand} and ResNet baselines across all datasets. For instance, on ACDC, CineMA achieved a ROC AUC of 97.98 (96.1–99.31)%, compared to 81.05 (75.69–86.56)% with ResNet and 63.08 (57.42–70.75)% with CineMA^{Rand}. The confusion matrices in Figure 4a show that CineMA yielded higher overall classification accuracy, whereas ResNet frequently misclassified normal patients as having an abnormal right ventricle. CineMA^{Rand} demonstrated poor diagnostic precision, often assigning most cases to myocardial infarction or dilated cardiomyopathy. The confusion matrices on other datasets were shown in Figure D.12.

To evaluate broader diagnostic performance, the datasets were combined into a binary classification of disease presence. Merging all disease subtype classes into one, CineMA achieved a substantially higher specificity of 60.06 (52.23–68.73)% compared to 31.55 (22.92–39.98)% with ResNet. Sensitivity also improved, rising to 90.20 (85.77–93.64)% from 86.84 (83.85–89.44)%. As shown in Figure 4b, CineMA consistently maintained a higher true positive rate (sensitivity) across varying false positive rates, achieving an overall AUC of 81.94% versus 66.23% for ResNet. This notable enhancement in diagnostic specificity suggests that CineMA could substantially reduce over-diagnosis while maintaining a low risk of false-negatives, positioning it as a promising tool for automated screening and triage in clinical CMR workflows.

3.5. CineMA achieved high accuracy on landmark localisation

For long-axis two-chamber and four-chamber views, valve and apical landmarks can be delineated to measure the mitral valvular plane and ventricular length. Using heatmap regression, in which the model predicts dense probability maps of landmarks, CineMA achieved an MAE for MAPSE of 0.66 (0.60–0.73) mm. Although higher than the UNet baseline error of 0.63 (0.56–0.70) mm, this difference (0.03 mm) is clinically negligible. For GLS, CineMA and UNet achieved identical MAEs of 1.28%, further supporting clinical equivalence between the two models in these functional measurements.

Localising landmarks via coordinate regression, which directly predicts landmark coordinates, was also evaluated. As shown in Figure D.14, while CineMA again outperformed the ResNet baseline, performance was generally lower than with heatmap regression, with a MAPSE MAE of 0.71 (0.63–0.76) mm and GLS MAE of 1.27 (1.13–1.4)%. Given its accuracy and interpretability, heatmap regression remains the preferred approach for landmark

localisation in cine CMR applications.

4. Discussion

We introduced CineMA, the first cine CMR foundation model to match or exceed convolutional neural networks trained from scratch across diverse clinical tasks. CineMA showed superior segmentation accuracy and more precise and consistent ejection fraction estimates, especially in low-data settings. CineMA also improved disease detection and diagnosis, with higher sensitivity and substantially better specificity, potentially reducing over-diagnosis. These results highlight the value of foundation models in delivering strong and generalisable performance across multiple applications with a single pre-trained model, suggesting readiness for real-world deployment.

This study offers key advantages over existing cardiac foundation models [9, 10, 11] beyond performance. First, it supports a broader range of tasks. Second, it evaluates prediction consistency and sample efficiency—two critical factors for clinical deployment—that were not addressed in prior work. Finally, releasing all code and model weights promotes reproducibility and clinical translation.

Nevertheless, there exist several limitations. First, although CineMA was evaluated across wide-ranging tasks, it was not assessed on predicting clinical outcomes such as major adverse cardiovascular events or mortality. Second, CineMA was pre-trained exclusively on cine CMR images; its performance on other modalities, such as LGE and T1 mapping, remains limited. Third, without using pre-trained weights, the proposed model did not consistently match convolutional architectures, highlighting opportunities for further refinement. Finally, training foundation models requires substantial computational resources, which remains a key barrier to the adoption of self-supervised pre-training in clinical settings.

CineMA demonstrates that fine-tuning foundation models can outperform traditional task-specific models in both accuracy and sample efficiency. By supporting multiple applications, CineMA offers a scalable, reproducible, and label-efficient solution for automated cine CMR analysis. The release of the full pipeline and model weights democratizes access to high-performance models that would otherwise require substantial computational resources, thereby lowering barriers to clinical and commercial adoption and enabling institutions globally to benefit from CineMA.

5. Acknowledgement

This research has been conducted using the UK Biobank Resource under Application Number 71702. The authors acknowledge the use of resources provided by the Isambard-AI National AI Research Resource (AIRR). Isambard-AI is operated by the University of Bristol and is funded by the UK Government's Department for Science, Innovation and Technology (DSIT) via UK Research and Innovation; and the Science and Technology Facilities Council [ST/AIRR/I-A-I/1023].

CM is directly and indirectly supported by the NIHR Biomedical Research Centres at University College London Hospital and Barts Health NHS Trusts. She is a co-founder of MycardiumAI.

During the preparation of this work, the authors used OpenAI's ChatGPT (GPT-4o) to improve language grammar. After using this tool/service, the authors reviewed and edited the content as needed and take full responsibility for the content of the publication.

6. Declaration of interest

The authors declare no competing interests.

Appendix A. Acronyms

2C	Two-chamber.
3C	Three-chamber.
4C	Four-chamber.
ACDC	Automated cardiac diagnosis challenge [14].
CI	Confidence interval.
CMR	Cardiac magnetic resonance.
CNN	Convolutional neural network.
CVD	Cardiovascular diseases.
EF	Ejection fraction.
EMIDEC	Evaluation of myocardial infarction from delayed-enhancement cardiac MRI [6].
GLS	Global longitudinal shortening.
Kaggle	Kaggle second annual data science bowl [17].
Landmark	Landmark detection in cardiac MRI by using a convolutional neural network [18].
LV	Left ventricle.
LVEF	Left ventricle ejection fraction.
M&Ms	Multi-centre, multi-vendor & multi-disease cardiac image segmentation challenge [15].
M&Ms2	Multi-disease, multi-view & multi-centre right ventricular segmentation in cardiac MRI [16].
MAE	Mean absolute error.
MAPSE	Mitral annular plane systolic excursion.
MyoPS2020	Myocardial pathology segmentation challenge 2020 [20].
Rescan	A multicenter, scan-rescan, human and machine learning CMR study to test generalisability and precision in imaging biomarker analysis [5].
ROC AUC	Area under the receiver operating characteristic curve.
RVEF	Right ventricle ejection fraction.
UKB	UK Biobank [6].

Appendix B. Data

All datasets used in this study, their associated views, labels, and target tasks have been summarised in Table B.2. The image resolution was standardised to $1 \times 1 \times 10$ mm for SAX and 1×1 mm for LAX views. All

Table B.2: Datasets and tasks. SAX=short-axis. LAX=long-axis. 2C=two-chamber. 3C=three-chamber. 4C=four-chamber. EF=Ejection Fraction. BMI=body mass index. n=total number of images.

Dataset	Modality	Views	n	Tasks
UKB [6]	Cine	SAX; LAX 2C/3C/4C	74,916	Pre-training.
ACDC [14]	Cine	SAX	150	Ventricle and myocardium segmentation; EF and BMI regression; Disease classification.
M&Ms [15]	Cine	SAX	375	Ventricle and myocardium segmentation; EF and age regression; Disease and sex classification.
M&Ms2 [16]	Cine	SAX; LAX 4C	360	Ventricle and myocardium segmentation; EF regression; Disease and vendor classification.
Kaggle [17]	Cine	SAX	1140	EF regression.
Rescan [5]	Cine	SAX	206	EF regression.
Landmark [18]	Cine	LAX 2C/4C	2,888	Landmark localisation.
EMIDEC [19]	LGE	SAX	100	Ventricle and scar segmentation.
Myops2020 [20]	LGE, T2, bSSFP	SAX	25	Scar segmentation.

images were then centre cropped or padded to a fixed spatial size of 192×192 for SAX and 256×256 for LAX. Centre cropping was performed either at the intersection of SAX, LAX 2C, and LAX 4C views when available, or at the anatomical centre of the left ventricle. Further task-specific details and dataset splits are described below.

Appendix B.1. UK Biobank

UK Biobank (UKB) dataset [6] included 74,916 studies, covering short-axis (SAX) and long-axis (LAX 2C, 3C, and 4C) views with 50 time frames each. These images were used for self-supervised pre-training only. Cropping was centred at the intersection of SAX and LAX views.

Appendix B.2. ACDC

Automated Cardiac Diagnosis Challenge (ACDC) [14] contained 100 training and 50 test SAX cine CMR scans, across five cardiovascular disease (CVD) categories: normal (NOR), myocardial infarction (MINF), dilated cardiomyopathy (DCM), hypertrophic cardiomyopathy (HCM), and abnormal right ventricle (ARV). Segmentation masks for left ventricle (LV), right ventricle (RV), and myocardium (MYO) were provided for end-diastolic (ED) and end-systolic (ES) frames. Ejection fraction (EF) was computed from these masks:

$$EF = \frac{EDV - ESV}{EDV} \times 100\%,$$

where EDV and ESV are end-diastolic and end-systolic volumes, respectively. Body mass index (BMI) labels were also available. Two samples per class were selected to form a 10-subject validation set. Images were cropped at the LV mask centre.

Appendix B.3. M&Ms

Multi-Centre, Multi-Vendor & Multi-Disease Cardiac Image Segmentation Challenge (M&Ms) [15] includes 375 SAX cine CMR scans: 175 for training, 40 for validation and 160 for testing. Seven disease subtype classes were present, including hypertrophic cardiomyopathy (HCM), dilated cardiomyopathy (DCM), hypertensive heart disease (HHD), abnormal right ventricle (ARV), athlete heart syndrome (AHS), ischemic heart disease (IHD), and left ventricle non-compaction (LVNC). Only frames at ED and ES phases were available, together with the segmentation labels of LV, RV, and MYO. EF was calculated from the segmentation masks. Additionally, the age for each patient was available. Images were cropped at the LV mask centre.

Appendix B.4. M&Ms 2

M&Ms-2 [16] dataset included 360 pairs of cine-MR images with SAX and LAX 4C views (160 training, 40 validation and 160 testing), distributed among 7 different disease subtype classes: dilated left ventricle (DLV), dilated right ventricle (DRV), hypertrophic cardiomyopathy (HCM), arrhythmogenic cardiomyopathy (ARR), tetralogy of fallot (FALL), inter-atrial communication (CIA), and tricuspid regurgitation (TRI). Only frames at ED and ES phases were available, together with the segmentation labels of LV, RV, and MYO. EF was calculated from the segmentation masks. The vendor of the MR machine was available per image. Images were cropped at the LV mask centre.

Appendix B.5. Kaggle

Kaggle dataset [17] included 1,140 cine CMR scans (500 training, 200 validation, and 440 testing), with SAX, LAX 2C, and LAX 4C views. LVEF volumes at ED and ES were provided in the training and validation sets. No segmentation masks were available. Cropping was centred at the SAX/LAX intersection. Only the test split was used for zero-shot evaluation.

Appendix B.6. Rescan

Rescan dataset [5] contained paired cine CMR scans (SAX, LAX 2C, LAX 4C) for 103 studies acquired at two time points. In 96% of cases, the interval between scans was within one week. LVEF was derived from the volume estimated at ED and ES by experts. Cropping was performed at the SAX/LAX intersection.

Appendix B.7. Landmark

Landmark localisation dataset [18] contains 2,888 LAX 2C and 4C images from 1,444 studies at ED and ES phases. The data were randomly split into training (60%), validation (20%), and test (20%) sets. Mitral annular plane systolic excursion (MAPSE) and global longitudinal shortening (GLS) were derived from ground truth coordinates. Heatmap labels were generated using a Gaussian kernel with $\sigma = 3$:

$$\text{heatmap}(x, y; x_i, y_i) = \exp\left(-\frac{(x - x_i)^2 + (y - y_i)^2}{2\sigma^2}\right)$$

where x_i and y_i are ground truth coordinates of the i -th landmark, with $i = 1, 2, 3$.

Appendix B.8. EMIDEC

EMIDEC dataset [19] consists of 100 training (33 normal cases and 67 pathological cases) and 50 testing DE-MRI images. The segmentation labels of myocardium, cavity, myocardial infarction and no-reflow are provided for training only. Therefore, 100 training images were randomly split into 60, 20, and 20 images, stratified by disease subtype classes. Images were centre-cropped at the cavity centre.

Appendix B.9. Myops2020

MyoPS2020 dataset [20] consists of 25 training and 20 testing studies. Each subject includes late gadolinium enhancement (LGE) CMR, the T2-weighted CMR, and the balanced-steady state free precession (bSSFP). The segmentation labels of LV blood pool, right ventricular blood pool, LV normal myocardium, LV myocardial edema, and LV myocardial scars were provided. Images were centre cropped at the left ventricular centre. The evaluation was performed using the provided software.

Appendix C. Model Development

Appendix C.1. CineMA model architecture

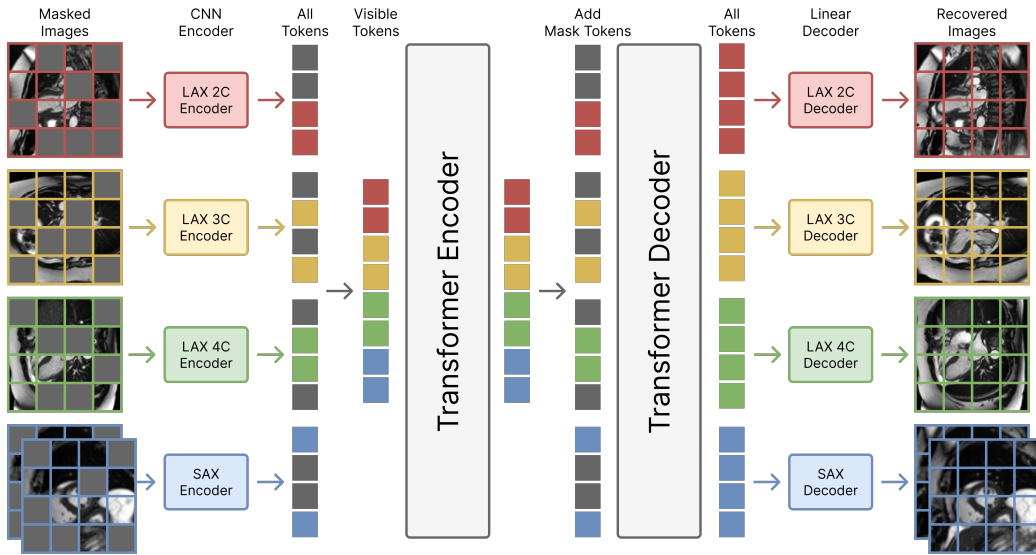


Figure C.5: CineMA model architecture. SAX=short-axis. LAX=long-axis. 2C=two-chamber. 3C=three-chamber. 4C=four-chamber.

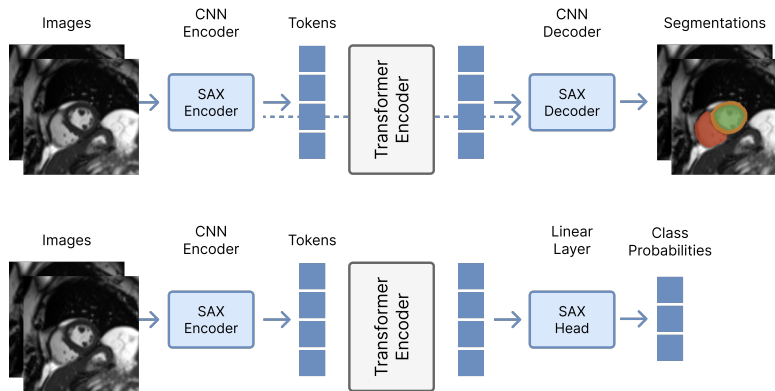


Figure C.6: Fine-tuned CineMA architectures for classification and segmentation. SAX=short-axis. CNN=convolutional neural network.

CineMA adopts an autoencoder architecture that takes four views: two-chamber, three-chamber, and four-chamber LAX views and SAX views. The

LAX views are two-dimensional of size (256, 256) and SAX views are three-dimensional of size (192, 192, 16). Each view is first split into patches of size (16, 16), with the SAX view using a depth-wise patch size of 1. A fixed proportion (75%) of patches are randomly masked by setting them to zero. The input images are then encoded using convolutional downsampling, reducing the spatial dimensions by a factor of $8\times$. The downsampled features are split into non-overlapping (2, 2) patches and embedded into feature tokens. Each masked patch corresponds to a single feature token, allowing tokens to be categorised into two groups: visible tokens (unmasked patches) and masked tokens (to be predicted). The visible tokens from all views are concatenated and passed through a shared Vision Transformer encoder. The encoded representations are then combined with masked tokens and processed by a shared Transformer decoder to reconstruct the masked patches. An illustration is provided in Figure C.5. In this study, CinaMA adopted the “base” configuration from MAE [12], leading to a model of 126 million parameters.

For downstream fine-tuning, encoder branches corresponding to unavailable views and all decoder layers were removed. Task-specific heads were added: a UNetR-style architecture [26] was employed for segmentation, and linear prediction layers were used for classification and regression tasks, as illustrated in Figure C.6. The model size varied depending on the input views and task type. For SAX images, the segmentation and classification models contained approximately 127 million and 90 million parameters, respectively. For LAX images, the corresponding number of parameters was approximately 102 million for segmentation and 88 million for classification. Regression models had comparable parameter counts to their classification counterparts.

Appendix C.2. Baseline convolutional neural networks

For tabular labels such as EF regression and disease subtype classification, 2D and 3D versions of ResNet50 were used as baseline models for SAX and LAX images, respectively. The 2D ResNet50 contained approximately 24 million parameters, while the 3D ResNet50 included around 46 million parameters. For dense prediction tasks such as segmentation and heatmap regression, five-layer UNet models with residual connections were employed, using channel widths of [32, 64, 128, 256, 512] at each layer—matching the configuration used in CineMA. The 2D UNet comprised approximately 27 million parameters, whereas the 3D UNet model included around 77 million parameters.

Appendix C.3. CineMA pre-training

CineMA was trained for 800 epochs on over 74,916 samples from the UK Biobank database [6] using LAX 2C, LAX 3C, LAX 4C, and SAX views. For each sample, a single time frame was randomly selected from 50 frames, followed by random gamma augmentation. Independent random affine transformations, including rotation, zooming, shearing, and shifting, were then applied to each view. The batch size was set to 128, and the learning rate schedule consisted of a linear warm-up over the first 10 epochs from 0 to 0.001, followed by a cosine decay to 10^{-6} . The model was trained on a mean squared error loss on the masked patches using the AdamW optimiser with betas (0.9, 0.95). Gradients were clipped with a maximum norm of 5.0.

Appendix C.4. Downstream model training

For downstream tasks, each model was trained three times with different random seeds on either the full dataset or a subset. Unstable training was discarded. If the training dataset was a subset, the subsets varied across random seeds, while the validation set remained unchanged. Data augmentation techniques included random gamma adjustment, random scaling, and random affine transformations for all tasks. For classification, label smoothing was applied, while for segmentation, random image dropout was used. Training was stopped early based on validation performance, and hyperparameters, listed in Table C.3, were identical across models and were not tuned via exhaustive search.

Appendix C.5. Implementation

The models were implemented using the Pytorch framework and MONAI framework [28], and the code is released at <https://github.com/mathpluscode/CineMA> under an MIT license.

Table C.3: Hyperparameters for downstream task model training. If the training dataset size is smaller than the preset batch size, the batch size is reduced to the closest power of two. CE=Cross-Entropy Loss. MSE=Mean Squared Error. MCC=Matthews Correlation Coefficient.

Hyperparameter	Classification	Regression	Segmentation
Total Epochs	800	800	4000
Warmup Epochs	10	10	50
Peak Learning Rate	0.001	0.001	0.001
End Learning Rate	10^{-5}	10^{-5}	10^{-5}
Batch Size	64	64	64
Loss	CE Loss	MSE	Dice Loss + CE Loss
Validation Frequency	20	20	100
Validation Patience	5	5	5
Validation Metric	MCC	Absolute Error	Dice Score
Hyperparameter	Landmark localisation		
	Heatmap	Coordinate	
Total Epochs	400	400	
Warmup Epochs	10	10	
Peak Learning Rate	0.001	0.001	
End Learning Rate	10^{-5}	10^{-5}	
Batch Size	64	64	
Loss	Dice Loss + CE Loss	Wing Loss [27]	
Validation Frequency	20	20	
Validation Patience	5	5	
Validation Metric	L^2 distance	L^2 distance	

Appendix D. Results

Appendix D.1. Ventricle and myocardium segmentation and EF regression

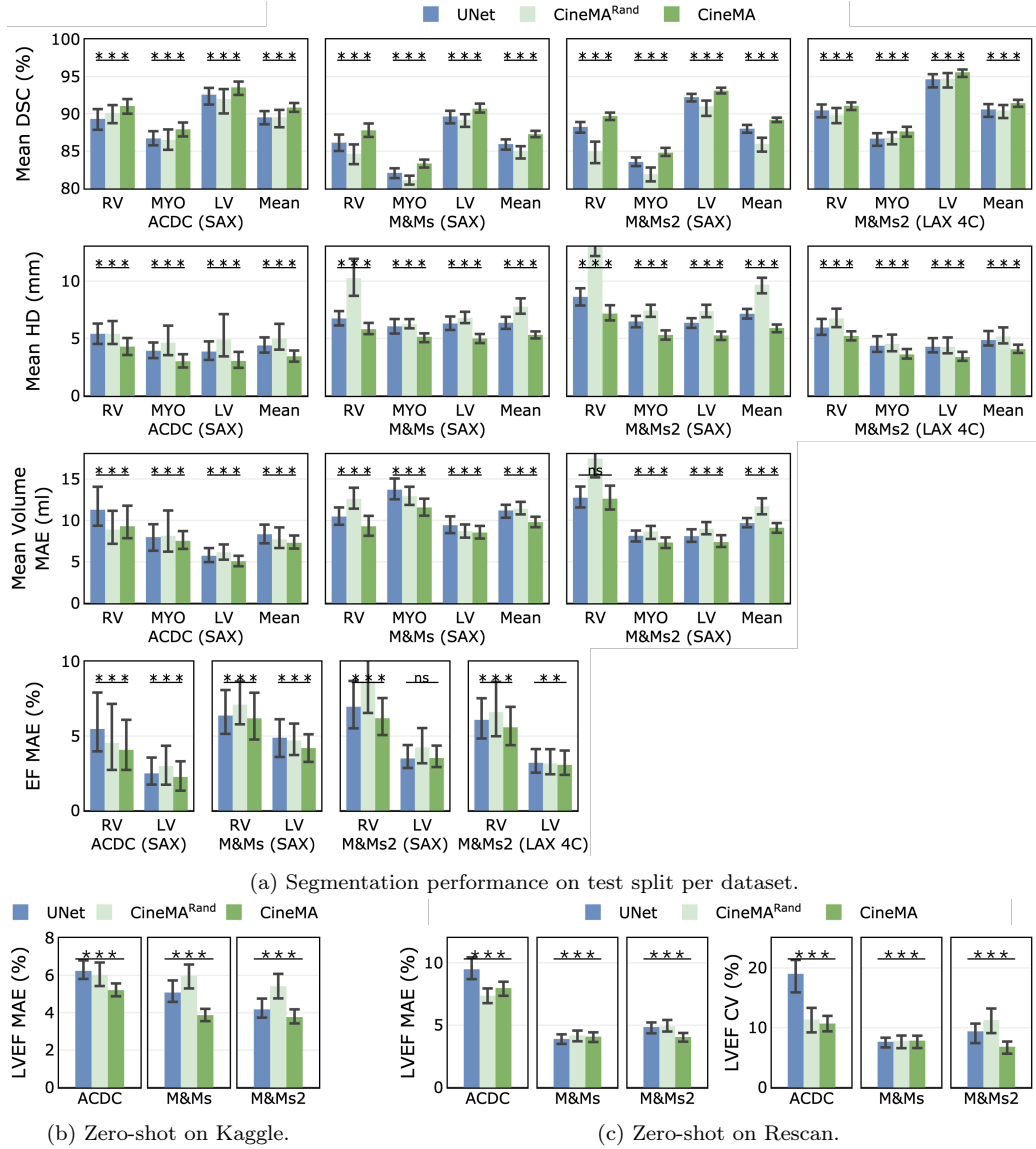
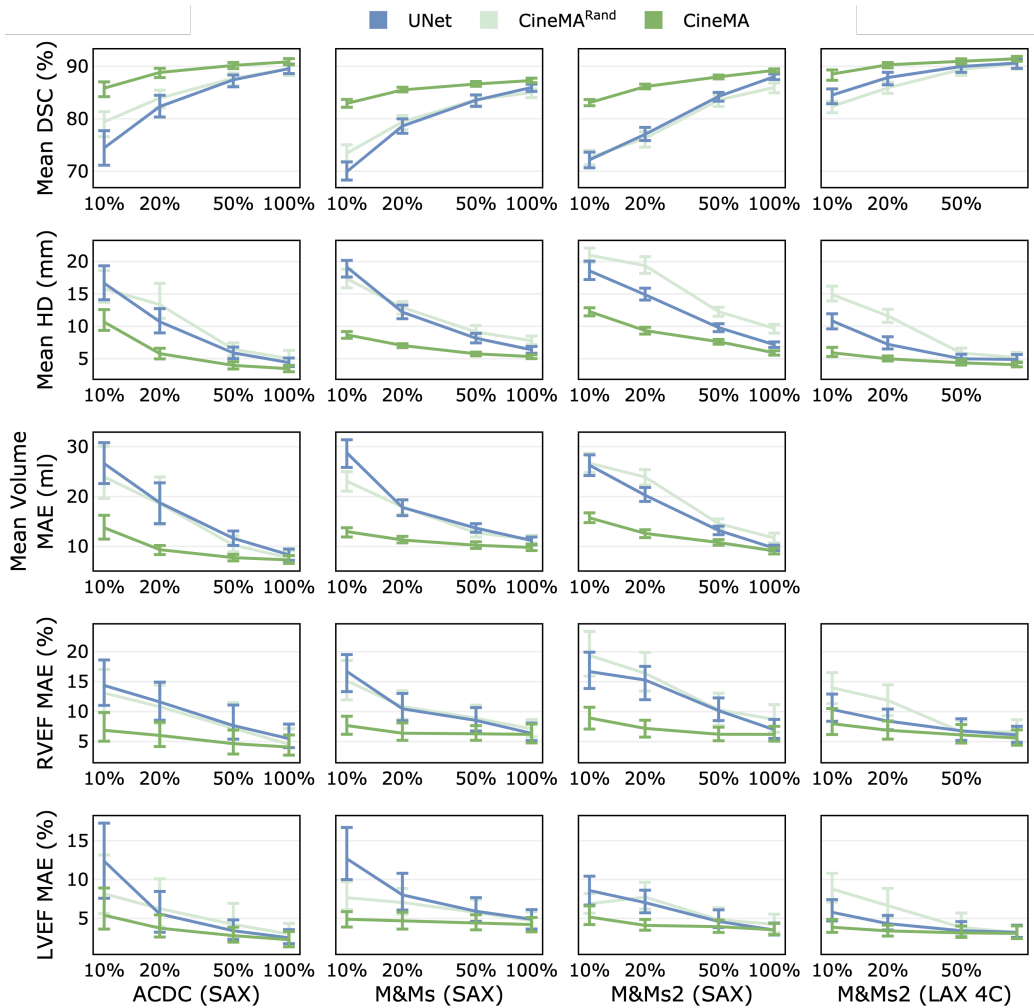
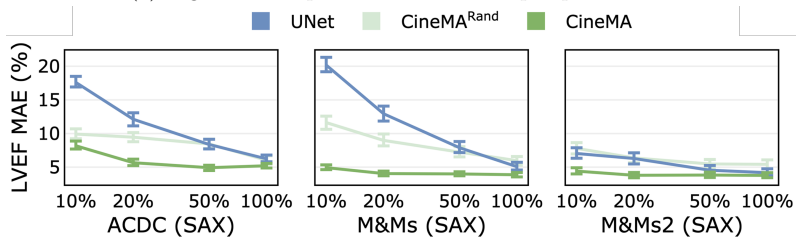


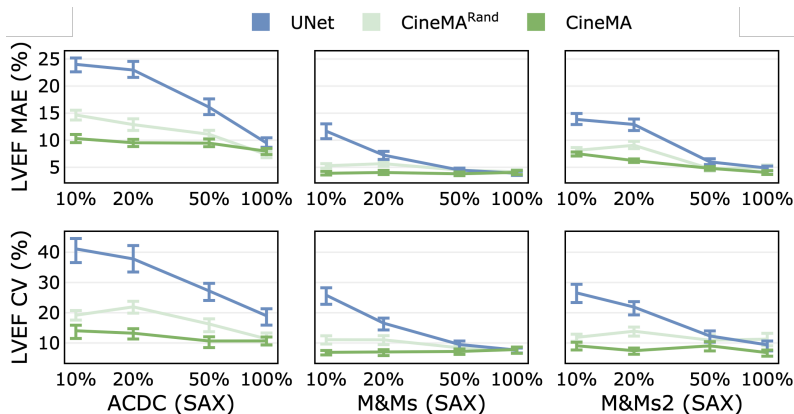
Figure D.7: Model comparison for segmentation on cine CMR images. SAX=short-axis. LAX=long-axis. DSC=Dice score. HD=95th percentile Hausdorff distance. RV=right ventricle. MYO=myocardium. LV=left ventricle. CV=coefficient of variation. MAE=mean absolute error.



(a) Segmentation performance on test split per dataset.



(b) Zero-shot on Kaggle.



(c) Zero-shot segmentation performance on rescan dataset test split.

Figure D.8: Segmentation performance on cine CMR images with different training data sizes. UNet and CineMA^{Rand} were trained from random initialisation, while CineMA was fine-tuned. SAX=short-axis. LAX=long-axis. DSC=Dice score. HD=95th percentile Hausdorff distance. RV=right ventricle. MYO=myocardium. LV=left ventricle. EF=ejection fraction. CV=coefficient of variation.

Figure D.7a compares segmentation model performance on the test splits of each dataset (also listed in Table D.4), including the mean absolute error (MAE) of ventricle volumes and EF estimated from segmentation outputs (see Table D.5). CineMA outperformed both UNet and CineMA^{Rand} across all evaluation metrics. Figure D.7b and Figure D.7c present the segmentation models' performance in estimating LVEF on Kaggle and Rescan datasets, which represent out-of-distribution samples not seen during pre-training or fine-tuning. CineMA achieved the lowest EF prediction error and highest consistency compared to both baselines (see Table D.6). Empirically, we observed that all LAX-based segmentation models produced approximately 15% EF error on out-of-distribution data, substantially higher than SAX-based ones. Their results were thus omitted.

In addition, Figure D.8 shows segmentation model performance under reduced training data conditions. CineMA consistently achieved higher segmentation accuracy and lower EF regression errors across all datasets, including the out-of-distribution Kaggle and Rescan datasets.

Dataset	Model	Dice Score (%)				95% Hausdorff Distance (mm)			
		RV	MYO	LV	Mean	RV	MYO	LV	Mean
ACDC (SAX)	UNet	89.33	86.71	92.58	89.54	5.41	3.93	3.86	4.40
	CineMA ^{Rand}	90.14	86.51	91.98	89.54	5.41	4.64	4.92	5.01
	CineMA	91.06	87.93	93.56	90.85	4.29	3.02	3.04	3.45
M&Ms (SAX)	UNet	86.14	82.09	89.66	85.96	6.75	6.06	6.31	6.37
	CineMA ^{Rand}	84.65	81.12	89.23	85.00	10.26	6.25	6.80	7.77
	CineMA	87.80	83.35	90.70	87.28	5.81	5.15	5.00	5.32
M&Ms2 (SAX)	UNet	88.26	83.56	92.25	88.02	8.63	6.49	6.37	7.16
	CineMA ^{Rand}	84.99	81.91	91.02	85.97	14.08	7.44	7.39	9.69
	CineMA	89.72	84.80	93.12	89.21	7.17	5.31	5.27	5.91
M&Ms2 (LAX 4C)	UNet	90.48	86.69	94.64	90.60	5.96	4.37	4.28	4.87
	CineMA ^{Rand}	89.83	86.81	94.72	90.45	6.75	4.52	4.26	5.17
	CineMA	91.09	87.64	95.59	91.44	5.22	3.61	3.39	4.07

Dataset	Model	Volume MAE (ml)			
		RV	MYO	LV	Mean
ACDC (SAX)	UNet	11.29	7.98	5.73	8.33
	CineMA ^{Rand}	8.89	8.13	6.16	7.72
	CineMA	9.30	7.53	5.07	7.30
M&Ms (SAX)	UNet	10.47	13.71	9.42	11.20
	CineMA ^{Rand}	12.60	12.92	8.71	11.41
	CineMA	9.29	11.57	8.54	9.80
M&Ms2 (SAX)	UNet	12.75	8.15	8.10	9.67
	CineMA ^{Rand}	17.47	8.66	9.00	11.71
	CineMA	12.62	7.33	7.39	9.12

Table D.4: Ventricle and myocardium segmentation performance. SAX=short-axis. LAX=long-axis. 4C=four-chamber. RV=right ventricle. MYO=myocardium. LV=left ventricle. MAE=mean absolute error.

Dataset	Model	LVEF MAE (%)	RVEF MAE (%)
ACDC (SAX)	UNet	2.50	5.48
	CineMA ^{Rand}	2.99	4.54
	CineMA	2.26	4.08
M&Ms (SAX)	UNet	4.89	6.38
	CineMA ^{Rand}	4.71	7.11
	CineMA	4.20	6.19
M&Ms2 (SAX)	UNet	3.50	6.97
	CineMA ^{Rand}	4.24	8.70
	CineMA	3.53	6.20
M&Ms2 (LAX 4C)	UNet	3.21	6.09
	CineMA ^{Rand}	3.17	6.61
	CineMA	3.07	5.59

Table D.5: Segmentation models' EF regression performance. SAX=short-axis. LAX=long-axis. 4C=four-chamber. RV=right ventricle. LV=left ventricle. EF=ejection fraction. MAE=mean absolute error.

Dataset	Model	Kaggle	Rescan	
		MAE (%)	MAE (%)	CV (%)
ACDC	UNet	6.24	9.49	19.01
	CineMA ^{Rand}	6.03	7.36	11.38
	CineMA	5.21	7.98	10.70
M&Ms	UNet	5.08	3.90	7.65
	CineMA ^{Rand}	5.98	4.18	7.82
	CineMA	3.87	4.08	7.84
M&Ms2	UNet	4.18	4.86	9.39
	CineMA ^{Rand}	5.42	4.92	11.27
	CineMA	3.77	4.05	6.82

Table D.6: Segmentation models’ zero-shot performance on left ventricle ejection fraction regression. Models were trained on ACDC, M&Ms, and M&Ms2, respectively, then evaluated on Kaggle and Rescan. MAE=mean absolute error. CV=coefficient of variation.

Appendix D.2. Scar segmentation

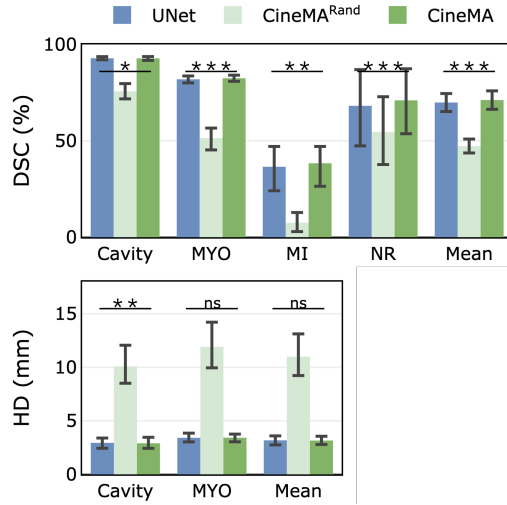
Model	Dice Score (%)					95% Hausdorff Distance (mm)		
	Cavity	MYO	MI	NR	Mean	Cavity	MYO	Mean
UNet	92.83	81.94	36.55	68.16	69.87	2.94	3.41	3.18
CineMA ^{Rand}	75.69	51.41	7.45	54.52	47.27	10.08	11.90	10.99
CineMA	92.76	82.48	38.36	70.99	71.15	2.90	3.42	3.16

Table D.7: Segmentation performance on EMIDEC. MYO=myocardium. MI=Myocardium infarction. NR=No-reflow.

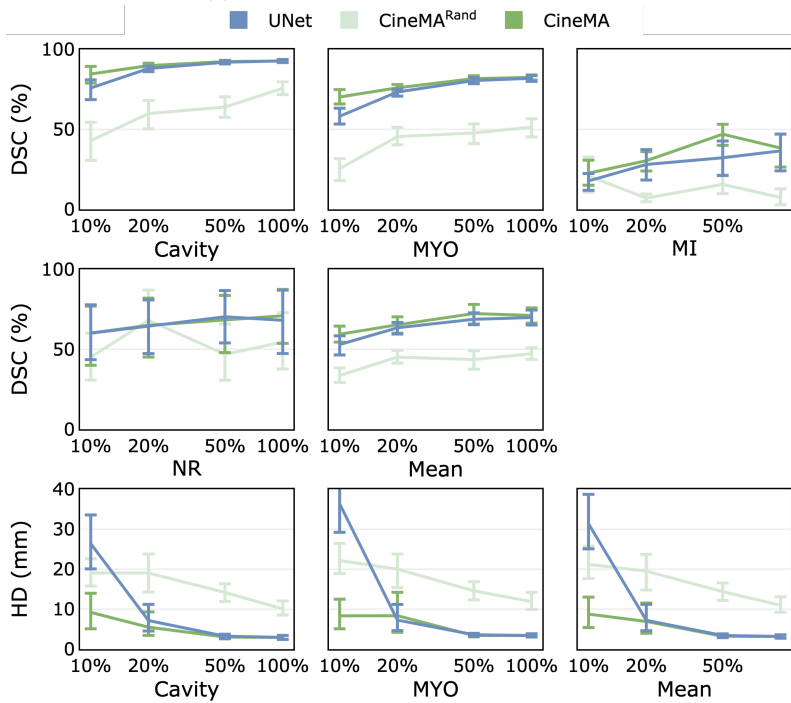
Model	Dice Score (%)		
	Scar	Edema Scar	Mean
UNet	55.24	58.74	56.99
CineMA ^{Rand}	52.45	59.82	56.14
CineMA	52.98	60.35	56.67

Table D.8: Segmentation performance on Myops2020.

Figure D.9 and Figure D.10 present segmentation model performance on the non-cine CMR datasets EMIDEC and MyoPS2020. Corresponding numerical results are provided in Table D.7 and Table D.8. Overall, CineMA outperformed the CineMA^{Rand} and achieved segmentation performance comparable to UNet.

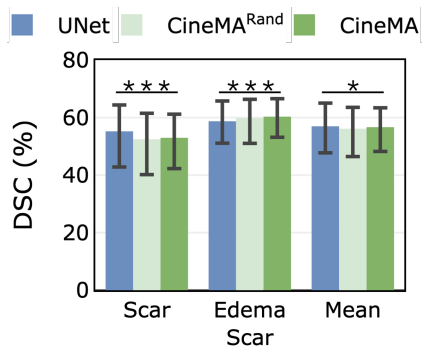


(a) Performance using full training data.

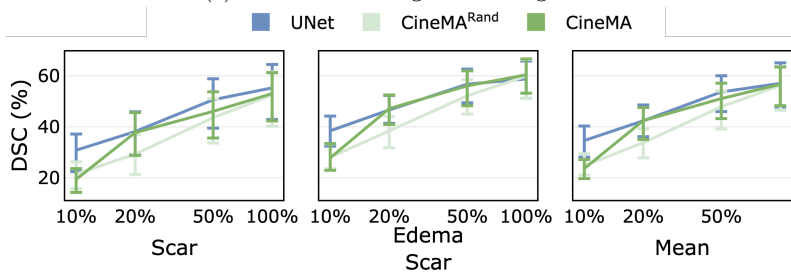


(b) Performance using different sizes of training data.

Figure D.9: Model comparison for segmentation on EMIDEC images. DSC=Dice score. HD=95% Hausdorff Distance. MYO=myocardium. MI=Myocardium infarction. NR=No-reflow.



(a) Performance using full training data.



(b) Performance using different sizes of training data.

Figure D.10: Model comparison for segmentation on Myops2020 images. DSC=Dice score. HD=95% Hausdorff Distance. MYO=myocardium. MI=Myocardium infarction. NR=No-reflow.

Appendix D.3. Classification of cardiovascular disease, patient sex, and MRI machine vendor

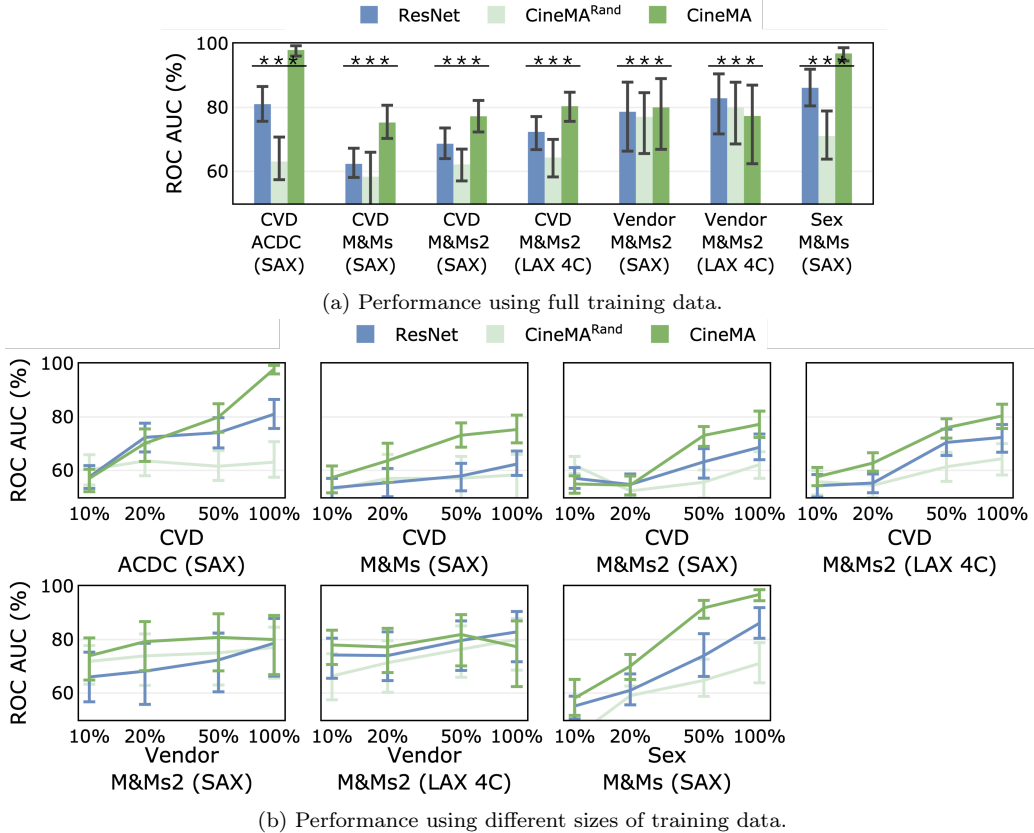
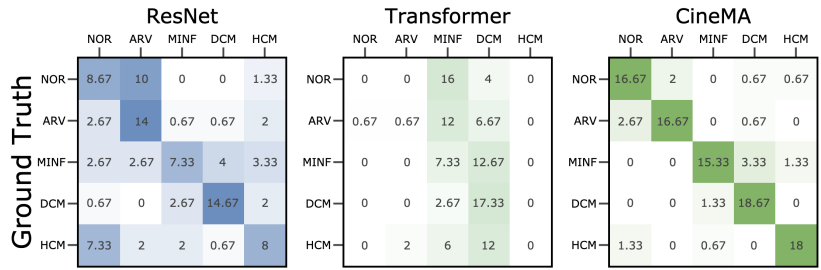
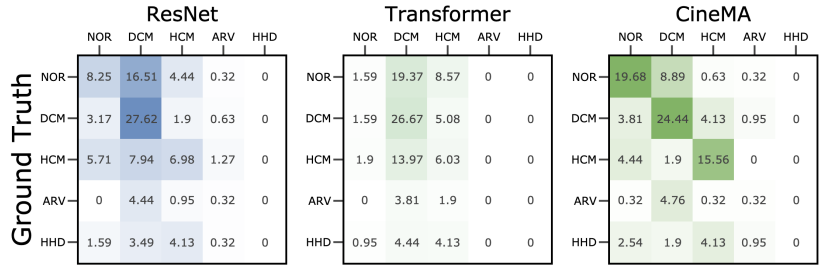


Figure D.11: Classification performance on cine CMR images. SAX=short-axis. LAX=long-axis. CVD=cardiovascular disease. EF=Ejection Fraction. BMI=Body Mass Index. ROC AUC=Area under the receiver operating characteristic curve.

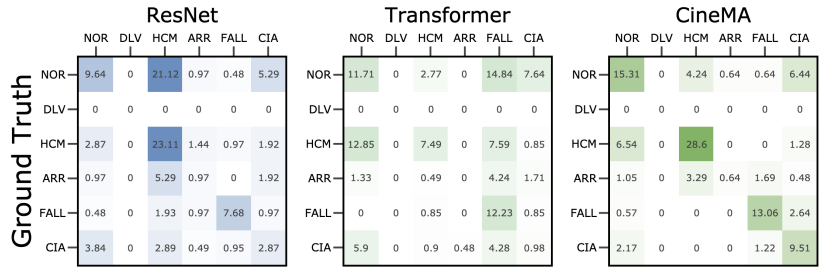
Figure D.11a summarises the performance comparison of CineMA with ResNet and CineMA^{Rand} models trained from random initialisation on various classification tasks, including disease subtype classification, patient sex classification, and MRI scanner vendor identification. For disease classification, the confusion matrices are illustrated in Figure D.12. Numerical results are provided in Table D.9 and Table D.10. CineMA consistently outperformed both baselines across all tasks except the vendor classification on the M&Ms2 dataset using LAX 4C view. Figure D.11b illustrates model performance under varying training data sizes. While CineMA remained the most accurate



(a) ACDC dataset.



(b) M&Ms dataset.



(c) M&Ms2 dataset.

Figure D.12: Cardiovascular disease classification confusion matrices. NOR=normal. ARV=abnormal right ventricle. MINF=myocardial infarction. DCM=dilated cardiomyopathy. HCM=hypertrophic cardiomyopathy. HHD=hypertensive heart disease. DLV=dilated left ventricle. ARR=arrhythmogenic cardiomyopathy. FALL=tetralogy of fallot. CIA=inter-atrial communication.

model overall, its relative advantage did not monotonically increase as the amount of training data decreased.

Data	Model	Classification		Detection	
		ROC AUC (%)	F1 (%)	Specificity (%)	Sensitivity (%)
ACDC (SAX)	ResNet	81.05	52.22	44.59	82.81
	CineMA ^{Rand}	63.08	25.13	0.00	99.16
	CineMA	97.98	85.36	83.03	94.87
M&Ms (SAX)	ResNet	62.36	43.28	27.40	85.43
	CineMA ^{Rand}	58.33	34.61	5.92	93.96
	CineMA	75.29	59.71	66.20	84.05
M&Ms2 (SAX)	ResNet	68.65	40.35	22.66	92.29
	CineMA ^{Rand}	62.18	29.98	29.12	77.13
	CineMA	77.25	54.15	30.96	91.69
M&Ms (LAX 4C)	ResNet	72.37	40.86	40.35	78.31
	CineMA ^{Rand}	64.35	33.17	32.16	74.65
	CineMA	80.41	53.37	31.73	92.02

Table D.9: Cardiovascular disease detection and classification performance. SAX=short-axis. LAX=long-axis. 4C=four-chamber. ROC AUC=Area under the receiver operating characteristic curve.

Target	Data	Model	ROC AUC (%)	F1 (%)
Vendor	M&Ms2 (SAX)	ResNet	78.66	74.97
		CineMA ^{Rand}	77.06	79.62
		CineMA	80.04	82.92
	M&Ms2 (LAX 4C)	ResNet	82.89	81.32
		CineMA ^{Rand}	80.06	77.84
		CineMA	77.35	81.27
Sex	M&Ms2 (SAX)	ResNet	86.17	70.24
		CineMA ^{Rand}	71.08	32.44
		CineMA	96.90	90.75

Table D.10: Cardiovascular disease detection and classification performance. SAX=short-axis. LAX=long-axis. 4C=four-chamber. ROC AUC=Area under the receiver operating characteristic curve.

Appendix D.4. Regression of EF, BMI and age

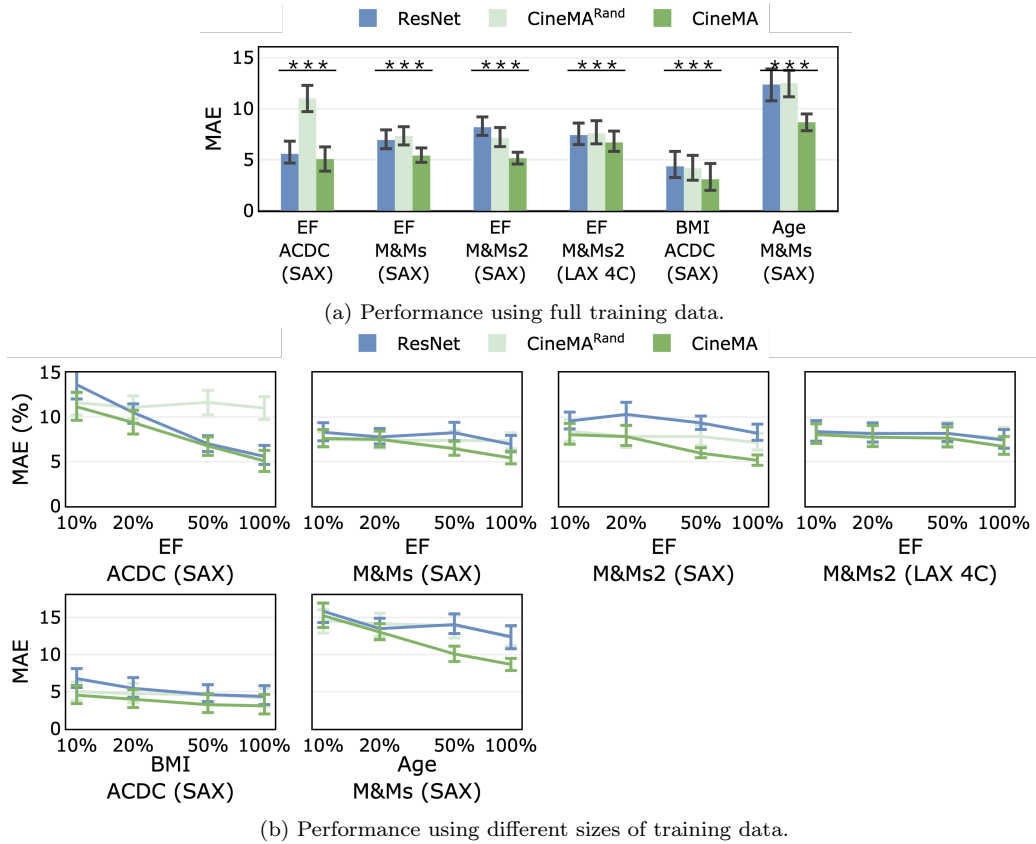


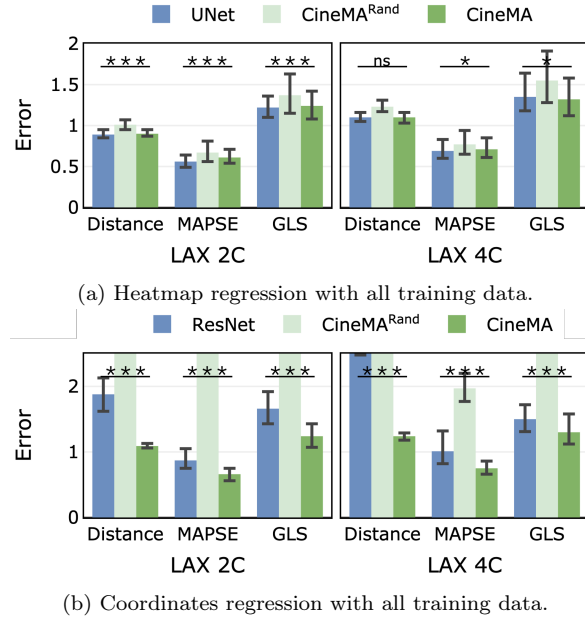
Figure D.13: Regression performance on cine CMR images. SAX=short-axis. LAX=long-axis. 4C=four-chamber. EF=Ejection Fraction. BMI=Body Mass Index. MAE=mean absolute error.

Figure D.13a summarises the comparison of CineMA with ResNet and CineMA^{Rand} models trained from random initialisation across multiple regression tasks, including ejection fraction, body mass index (BMI), and patient age prediction. CineMA consistently outperformed the baseline models on all tasks. Figure D.13b illustrates the effect of reducing training data on model performance. While CineMA maintained the highest predictive accuracy overall, the relative performance gap did not consistently widen as training data decreased.

Target	Data	Model	MAE
EF	ACDC (SAX)	ResNet	5.58
		CineMA ^{Rand}	11.01
		CineMA	5.07
	M&Ms (SAX)	ResNet	6.94
		CineMA ^{Rand}	7.33
		CineMA	5.41
	M&Ms2 (SAX)	ResNet	8.19
		CineMA ^{Rand}	7.13
		CineMA	5.15
	M&Ms2 (LAX 4C)	ResNet	7.42
		CineMA ^{Rand}	7.60
		CineMA	6.70
BMI	ACDC (SAX)	ResNet	4.36
		CineMA ^{Rand}	4.17
		CineMA	3.09
Age	M&Ms (SAX)	ResNet	12.38
		CineMA ^{Rand}	12.51
		CineMA	8.68

Table D.11: Regression performance on cine CMR images. SAX=short-axis. LAX=long-axis. 4C=four-chamber. EF=Ejection Fraction. BMI=Body Mass Index. MAE=mean absolute error.

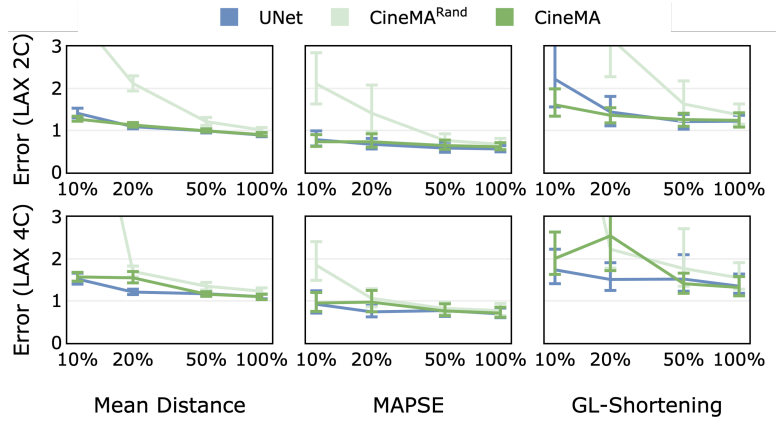
Appendix D.5. Landmark localisation



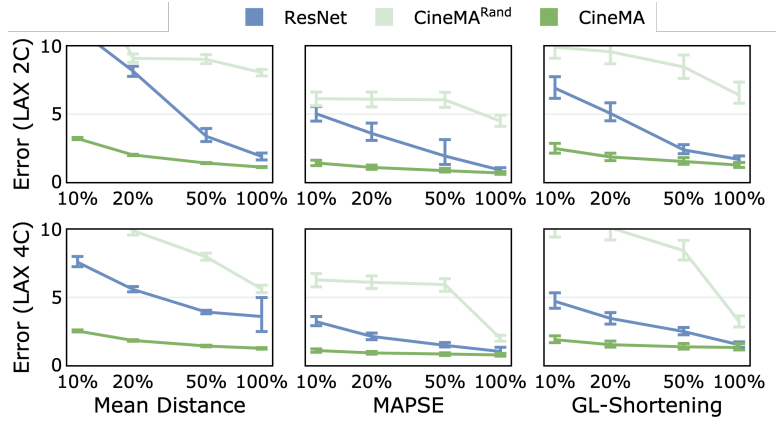
Method	View	Model	Euclidean Distance (mm)				MAE (%)	
			Valve1	Valve2	Apex	Mean	MAPSE	GLS
Heatmap	LAX 2C	UNet	0.85	0.90	0.93	0.89	0.56	1.22
		CineMA ^{Rand}	0.93	1.00	1.10	1.01	0.67	1.37
		CineMA	0.83	0.89	0.99	0.90	0.61	1.24
	LAX 4C	UNet	0.98	1.25	1.07	1.10	0.69	1.35
		CineMA ^{Rand}	1.13	1.31	1.26	1.23	0.77	1.55
		CineMA	0.99	1.24	1.06	1.10	0.71	1.32
Coordinates	LAX 2C	ResNet	1.88	1.88	1.87	1.88	0.87	1.66
		CineMA ^{Rand}	7.96	7.90	8.37	8.07	4.49	6.41
		CineMA	1.06	1.13	1.09	1.09	0.66	1.24
	LAX 4C	ResNet	1.99	4.18	4.60	3.59	1.01	1.50
		CineMA ^{Rand}	5.61	5.48	5.78	5.62	1.97	3.22
		CineMA	1.18	1.39	1.14	1.24	0.75	1.30

Table D.12: Landmark localisation performance using heatmap or coordinates regression. MAE=mean absolute error. LAX=long-axis. 2C=two-chamber. 4C=four-chamber. MAPSE = mitral annular plane systolic excursion. GLS=global longitudinal shortening.

Figure D.14a and Figure D.14c summarise the comparison between fine-tuned CineMA and UNet and CineMA^{Rand} models trained from random initialisation for landmark localisation using heatmap regression. CineMA



(c) Heatmap regression with different sizes of training data.



(d) Coordinates regression with different sizes of training data.

Figure D.14: Model comparison for landmark localisation on cine CMR images in LAX views. LAX=long-axis. 2C=two-chamber. 4C=four-chamber. MAPSE = mitral annular plane systolic excursion. GL-Shortening=global longitudinal shortening.

achieved performance comparable to UNet and consistently outperformed CineMA^{Rand}, both when trained on the full dataset and reduced subsets. Detailed metric values for models trained with the full dataset are also summarised in Table D.12.

Figure D.14b and Figure D.14d present results for coordinate regression. CineMA outperformed both UNet and CineMA^{Rand} across all settings. Notably, the performance gap between CineMA and the baseline models widened as the amount of training data decreased, highlighting CineMA’s superior data efficiency in coordinate-based landmark localisation.

References

- [1] G. A. Mensah, G. A. Roth, V. Fuster, The global burden of cardiovascular diseases and risk factors: 2020 and beyond, 2019.
- [2] P. S. Rajiah, C. J. François, T. Leiner, Cardiac mri: state of the art, *Radiology* 307 (2023) e223008.
- [3] F. von Knobelsdorff-Brenkenhoff, J. Schulz-Menger, Cardiovascular magnetic resonance in the guidelines of the european society of cardiology: a comprehensive summary and update, *Journal of Cardiovascular Magnetic Resonance* 25 (2023) 42.
- [4] C. M. Kramer, J. Barkhausen, C. Bucciarelli-Ducci, S. D. Flamm, R. J. Kim, E. Nagel, Standardized cardiovascular magnetic resonance imaging (cmr) protocols: 2020 update, *Journal of Cardiovascular Magnetic Resonance* 22 (2020) 17.
- [5] A. N. Bhuya, W. Bai, C. Lau, R. H. Davies, Y. Ye, H. Bulluck, E. McAlindon, V. Culotta, P. P. Swoboda, G. Captur, et al., A multicenter, scan-rescan, human and machine learning cmr study to test generalizability and precision in imaging biomarker analysis, *Circulation: Cardiovascular Imaging* 12 (2019) e009214.
- [6] Z. Raisi-Estabragh, N. C. Harvey, S. Neubauer, S. E. Petersen, Cardiovascular magnetic resonance imaging in the uk biobank: a major international health research resource, *European Heart Journal-Cardiovascular Imaging* 22 (2021) 251–258.
- [7] R. Bommasani, D. A. Hudson, E. Adeli, R. Altman, S. Arora, S. von Arx, M. S. Bernstein, J. Bohg, A. Bosselut, E. Brunskill, et al., On the opportunities and risks of foundation models, *arXiv preprint arXiv:2108.07258* (2021).
- [8] J. Ma, Y. He, F. Li, L. Han, C. You, B. Wang, Segment anything in medical images, *Nature Communications* 15 (2024) 654.
- [9] R. Shad, C. Zakka, D. Kaur, R. Fong, R. W. Filice, J. Mongan, K. Kalianos, N. Khandwala, D. Eng, M. Leipzig, et al., A generalizable deep learning system for cardiac mri, *arXiv preprint arXiv:2312.00357* (2023).

- [10] A. J. Jacob, I. Borgohain, T. Chitiboi, P. Sharma, D. Comaniciu, D. Rueckert, Towards a vision foundation model for comprehensive assessment of cardiac mri, arXiv preprint arXiv:2410.01665 (2024).
- [11] Y. Zhang, P. Hager, C. Liu, S. Shit, C. Chen, D. Rueckert, J. Pan, Towards cardiac mri foundation models: Comprehensive visual-tabular representations for whole-heart assessment and beyond, arXiv preprint arXiv:2504.13037 (2025).
- [12] K. He, X. Chen, S. Xie, Y. Li, P. Dollár, R. Girshick, Masked autoencoders are scalable vision learners, in: Proceedings of the IEEE/CVF conference on computer vision and pattern recognition, 2022, pp. 16000–16009.
- [13] E. Potter, T. H. Marwick, Assessment of left ventricular function by echocardiography: the case for routinely adding global longitudinal strain to ejection fraction, *JACC: Cardiovascular Imaging* 11 (2018) 260–274.
- [14] O. Bernard, A. Lalande, C. Zotti, F. Cervenansky, X. Yang, P.-A. Heng, I. Cetin, K. Lekadir, O. Camara, M. A. G. Ballester, et al., Deep learning techniques for automatic mri cardiac multi-structures segmentation and diagnosis: is the problem solved?, *IEEE transactions on medical imaging* 37 (2018) 2514–2525.
- [15] V. M. Campello, P. Gkontra, C. Izquierdo, C. Martín-Isla, A. Sojoudi, P. M. Full, K. Maier-Hein, Y. Zhang, Z. He, J. Ma, et al., Multi-centre, multi-vendor and multi-disease cardiac segmentation: the m&ms challenge, *IEEE Transactions on Medical Imaging* 40 (2021) 3543–3554.
- [16] C. Martín-Isla, V. M. Campello, C. Izquierdo, K. Kushibar, C. Sendra-Balcells, P. Gkontra, A. Sojoudi, M. J. Fulton, T. W. Arega, K. Punithakumar, et al., Deep learning segmentation of the right ventricle in cardiac mri: the m&ms challenge, *IEEE Journal of Biomedical and Health Informatics* 27 (2023) 3302–3313.
- [17] N. A, B. AJ, A. Andrew, M. Jonathan, B. Josette, V. Kung, O. Meghan, K. Mike, S. Roman, Shannon, M. Steve, C. Will, Second annual data science bowl, 2015. URL: <https://kaggle.com/competitions/second-annual-data-science-bowl>.

- [18] H. Xue, J. Artico, M. Fontana, J. C. Moon, R. H. Davies, P. Kellman, Landmark detection in cardiac mri by using a convolutional neural network, *Radiology: Artificial Intelligence* 3 (2021) e200197.
- [19] A. Lalande, Z. Chen, T. Decourselle, A. Qayyum, T. Pommier, L. Lorgis, E. de La Rosa, A. Cochet, Y. Cottin, D. Ginhac, et al., Emidec: a database usable for the automatic evaluation of myocardial infarction from delayed-enhancement cardiac mri, *Data* 5 (2020) 89.
- [20] L. Li, F. Wu, S. Wang, X. Luo, C. Martín-Isla, S. Zhai, J. Zhang, Y. Liu, Z. Zhang, M. J. Ankenbrand, et al., Myops: A benchmark of myocardial pathology segmentation combining three-sequence cardiac magnetic resonance images, *Medical Image Analysis* 87 (2023) 102808.
- [21] P. Gao, T. Ma, H. Li, Z. Lin, J. Dai, Y. Qiao, Convmae: Masked convolution meets masked autoencoders, *arXiv preprint arXiv:2205.03892* (2022).
- [22] R. Bachmann, D. Mizrahi, A. Atanov, A. Zamir, Multimaec: Multi-modal multi-task masked autoencoders, in: *European Conference on Computer Vision*, Springer, 2022, pp. 348–367.
- [23] S. Targ, D. Almeida, K. Lyman, Resnet in resnet: Generalizing residual architectures, *arXiv preprint arXiv:1603.08029* (2016).
- [24] S. McIntosh-Smith, S. R. Alam, C. Woods, Isambard-ai: a leadership class supercomputer optimised specifically for artificial intelligence, *arXiv preprint arXiv:2410.11199* (2024).
- [25] F. Isensee, P. F. Jaeger, S. A. Kohl, J. Petersen, K. H. Maier-Hein, nnu-net: a self-configuring method for deep learning-based biomedical image segmentation, *Nature methods* 18 (2021) 203–211.
- [26] A. Hatamizadeh, Y. Tang, V. Nath, D. Yang, A. Myronenko, B. Landman, H. R. Roth, D. Xu, Unetr: Transformers for 3d medical image segmentation, in: *Proceedings of the IEEE/CVF winter conference on applications of computer vision*, 2022, pp. 574–584.
- [27] Z.-H. Feng, J. Kittler, M. Awais, P. Huber, X.-J. Wu, Wing loss for robust facial landmark localisation with convolutional neural networks,

in: Proceedings of the IEEE conference on computer vision and pattern recognition, 2018, pp. 2235–2245.

- [28] M. J. Cardoso, W. Li, R. Brown, N. Ma, E. Kerfoot, Y. Wang, B. Murrey, A. Myronenko, C. Zhao, D. Yang, et al., Monai: An open-source framework for deep learning in healthcare, arXiv preprint arXiv:2211.02701 (2022).